



# Advanced degradation of organic pollutants using sonophotocatalytic peroxymonosulfate activation with CoFe<sub>2</sub>O<sub>4</sub>/Cu- and Ce-doped SnO<sub>2</sub> composites

Mokhtar Hjiri<sup>a,b</sup>, Roger Bujaldón<sup>c,d</sup>, Judit Lloreda<sup>c,d</sup>, Elvira Gómez<sup>c,d</sup>, Albert Serra<sup>c,d,\*</sup>

<sup>a</sup> Department of Physics, College of Sciences, Imam Mohammad Ibn Saud Islamic University (IMSIU), SA-11623, Riyadh, Saudi Arabia

<sup>b</sup> Laboratory of Physics of Materials and Nanomaterials Applied at Environment (LaPhyMNE), Faculty of Sciences in Gabes, Gabes University, TNSA-6079, Gabes, Tunisia

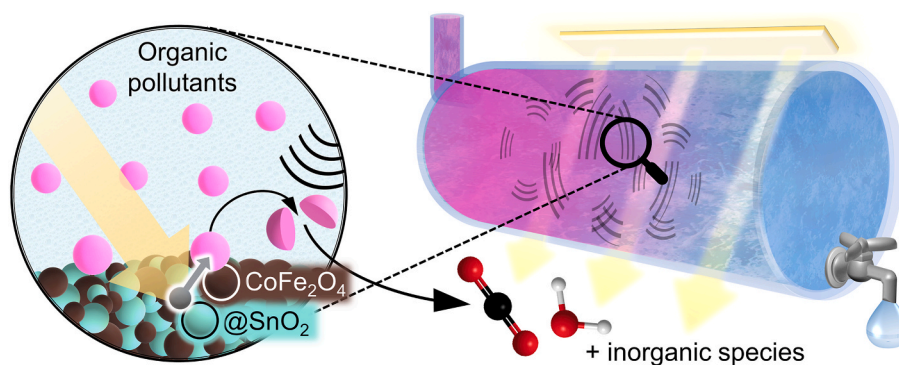
<sup>c</sup> Grup d'Electrodeposició de Capes Primes i Nanoestructures (GE-CPN), Departament de Ciència de Materials i Química Física, Universitat de Barcelona, Martí i Franquès, 1, E-08028, Barcelona, Catalonia, Spain

<sup>d</sup> Institute of Nanoscience and Nanotechnology (IN2UB), Universitat de Barcelona, Martí i Franquès, 1, E-08028, Barcelona, Catalonia, Spain

## HIGHLIGHTS

- CoFe<sub>2</sub>O<sub>4</sub>/Cu- and Ce-doped SnO<sub>2</sub> nanocomposites for sonophotocatalytic mineralization.
- The catalytic activity depends on the at. % of doping metal and the composition ratio.
- Complete degradation of Rhodamine B in 5 min with the optimized catalyst composition.
- Robust catalysts with structural stability and long-term reusability.
- High mineralization rates for a multi-contaminated solution of organic pollutants.

## GRAPHICAL ABSTRACT



## ARTICLE INFO

Handling editor: Dr. S Garcia-Segura

### Keywords:

Peroxymonosulfate (PMS)  
Sulfate radicals  
Sonophotocatalysis  
Water treatment  
Organic pollutants  
Nanocomposites

## ABSTRACT

The rampant upsurge of organic pollutants in aqueous media has become one of the major concerns nowadays. Finding non-specific catalysts that can target a wide range of organic pollutants is a key challenge. Eco-friendly oxidative radicals, such as promoted by peroxymonosulfate (PMS), are necessary for efficient water decontamination. We propose a multicomponent composite catalyst for activating PMS using a dual strategy of sonophotocatalysis. The composite integrates cobalt ferrite and Cu- or Ce-doped SnO<sub>2</sub>, with the at. % of doping metal and the mixture ratio carefully balanced. The top-performing architectures were able to decompose rhodamine B (20 ppm), a representative pollutant, in under 3 min and achieve over 70% mineralization in just 5 min. The synthesized nanocomposites demonstrated exceptional sonophotocatalytic performance, even when treating complex and diverse multipollutant solutions (80 ppm), achieving over 75% mineralization after 150 min.

\* Corresponding author. Grup d'Electrodeposició de Capes Primes i Nanoestructures (GE-CPN), Departament de Ciència de Materials i Química Física, Universitat de Barcelona, Martí i Franquès, 1, E-08028, Barcelona, Catalonia, Spain.

E-mail address: [a.serra@ub.edu](mailto:a.serra@ub.edu) (A. Serra).

<https://doi.org/10.1016/j.chemosphere.2024.141656>

Received 17 January 2024; Received in revised form 21 February 2024; Accepted 5 March 2024

Available online 9 March 2024

0045-6535/© 2024 The Authors. Published by Elsevier Ltd. This is an open access article under the CC BY license (<http://creativecommons.org/licenses/by/4.0/>).

Considering their high stability and reusability, the proposed  $\text{CoFe}_2\text{O}_4/\text{Cu}$ - and Ce-doped  $\text{SnO}_2$  materials are among the state-of-the-art heterogeneous catalysts for mineralizing organic pollutants through PMS activation.

## 1. Introduction

In recent decades, the discharge of emerging organic pollutants into the environment has become widespread. These pollutants originate from industrial, agricultural, and pharmaceutical activities. This has raised concerns due to their persistence, potential toxicity, and limited understanding of their long-term effects on aquatic ecosystems and human health (Gómez et al., 2022; Lee et al., 2016; Sayadi et al., 2019). Water pollution is a major problem in underdeveloped countries due to various factors, including inadequate sanitation infrastructure, lax environmental regulations, rapid urbanization and population growth, low awareness of proper waste management, and improper agricultural practices such as pesticide use (Kanakaraju et al., 2018; Serrà et al., 2020a,b; S. M. Wang et al., 2023). Furthermore, traditional water treatment methods can be expensive and may not adequately address the persistent and diverse nature of these pollutants. To tackle the difficulties associated with emerging organic contaminants, cooperation among scientific, regulatory, and societal entities is necessary (Serrà et al., 2020a,b; Tayyab et al., 2023; Wang et al., 2022a,b, 2024).

Advanced oxidation processes (AOPs) have gained significant attention due to their effectiveness in removing a wide range of pollutants, including organic, inorganic, and biological compounds (Brillas et al., 2021; Brillas and Garcia-Segura, 2023; Sayadi et al., 2019; Tayyab et al., 2022). AOPs rely on the generation of highly reactive hydroxyl radicals (1.8–2.7 V vs NHE, half-life: 1  $\mu\text{s}$ ) that rapidly oxidize organic compounds, leading their complete mineralization into carbon dioxide, water, and inorganic salts. It is worth noting that peroxymonosulfate (PMS) has been identified as a promising eco-friendly method for producing sulfate radicals in AOPs. These radicals have a potent oxidative power (2.5–3.1 V vs NHE) and a relatively longer half-life (30–40  $\mu\text{s}$ ) compared to hydroxyl radicals (Ni et al., 2022a; Pang et al., 2021; Qi et al., 2016; Wacławek et al., 2017; N. Wang et al., 2022a,b). Singlet oxygen, which is the dominant reactive oxygen species for oxidizing electron-rich organics through a nonradical pathway, is also formed by PMS activation (Giannakis et al., 2021; Yue et al., 2024). External factors, such as ultraviolet radiation, electrolysis, ultrasound, heating, or catalytic methods can trigger the activation of PMS (Bui et al., 2021; Ni et al., 2022b; Shang et al., 2023; Wacławek et al., 2017; W. Wang et al., 2022a,b). Despite the promising results, practical implementation of this technology requires cost reduction, improved efficiency, and scalability (Fedorov et al., 2020; Rahimzadeh et al., 2020; Taktastan et al., 2018; Xu et al., 2020). Sonophotocatalysis is a process that combines ultrasound-induced acoustic cavitation and catalyst photoexcitation to increase radical concentration. This is achieved through a synergistic effect resulting from the reduced band-gap due to heightened temperature and pressure from ultrasound, and improved charge carrier separation through internal electric field formation, which reduces recombination losses. Ultrasound-induced cavitation improves mass transfer between catalyst and liquid, maintains catalyst homogeneity, and cleans its surface (Bembibre et al., 2022; Diao et al., 2020). This dual strategy generates diverse highly reactive species, including sulfate and hydroxyl radicals, which significantly enhance its degradation potential (Barzegar et al., 2018; Rahimzadeh et al., 2020; Xu et al., 2020).

Recent research has shown that cobalt-based nanostructures are effective catalysts for activating PMS and generating sulfate radicals (Du et al., 2016; Ni et al., 2022a). However, the instability and poor reusability of most cobalt nanostructures hinder their efficiency and trigger the release of environmentally harmful  $\text{Co(II)}$ , which poses ecological risks due to its toxicity (Han et al., 2024; Ma et al., 2023; Peng et al., 2023; Yao et al., 2015). Cobalt ferrite ( $\text{CoFe}_2\text{O}_4$ ) is a promising option due to its semiconductor nature, narrow band gap, remarkable

optoelectronic properties, broad visible light absorption range, cost-effectiveness, photochemical stability, and inherent magnetic characteristics. These properties collectively enhance PMS activation for sulfate radical formation (Dai et al., 2023; Du et al., 2016; Xu et al., 2019; Yang et al., 2018; Zhang et al., 2023). In addition, the characteristics of magnetic nanoparticles make catalyst separation and reusability easier, which effectively addresses a major challenge in heterogeneous catalysis. However, cobalt ferrite has limitations in terms of organic compound mineralization rates and sustained medium-to-long-term activity, which could restrict its applicability (Dai et al., 2023; Du et al., 2016; Sun et al., 2023). Research suggests that the catalytic activity for organic compound mineralization can be substantially enhanced by combining tin oxide ( $\text{SnO}_2$ ), a semiconductor transition metal oxide, with other metal. This holds true for both purely photocatalytic processes and those reliant on PMS catalysis. This improvement arises from heightened charge separation, expanded light absorption range, and increased surface reactivity (Pang et al., 2021; S. Wang et al., 2023; Yang et al., 2023).

This study presents a comprehensive investigation into the advanced degradation of organic pollutants using a novel approach: the sonophotocatalytic heterogeneous activation of PMS facilitated by  $\text{CoFe}_2\text{O}_4/\text{Cu}$ - and Ce-doped  $\text{SnO}_2$  nanocomposites. This work contributes to the fundamental understanding of the underlying mechanisms and interactions involved in the complex system through a systematic exploration of the synthesis, characterization, and catalytic performance of the developed nanocomposites. The results presented here hold significant implications for the design and optimization of efficient and sustainable technologies for environmental remediation.

## 2. Experimental details

### 2.1. Synthesis of Cu- and Ce-doped $\text{SnO}_2$ particles

$\text{SnO}_2$ , Cu-doped  $\text{SnO}_2$ , and Ce-doped  $\text{SnO}_2$  nanoparticles were synthesized via a sol-gel process involving supercritical drying of ethanol. The procedure began with dissolving 16 g of tin precursor ( $\text{SnCl}_2 \cdot 6 \text{H}_2\text{O}$ ; 98%) in 112 mL of methanol. Copper chloride [ $\text{CuCl}_2$ , 99%] and cerium nitrate [ $\text{Ce}(\text{NO}_3)_3 \cdot 6 \text{H}_2\text{O}$ , 98%] were then added in appropriate quantities to achieve the desired copper and cerium doping concentrations (1, 3, and 5 at.%), respectively. The precursors were stirred until fully dissolved, resulting in a clear solution. The solution was then subjected to supercritical drying with ethanol to yield powdered aerogels. Finally, the samples underwent a 2-h calcination process at 500 °C.

### 2.2. Synthesis of $\text{CoFe}_2\text{O}_4$ nanoparticles

The synthesis of cobalt ferrite nanoparticles was achieved through a simple wet chemical co-precipitation method. In this standard procedure, a 50 mL of 0.4 M iron (II) chloride solution was combined with a 50 mL of 0.2 M cobalt chloride solution both prepared using Milli-Q water. The pH was then carefully monitored and adjusted to a pH level of 11–12 by gradually adding 25 mL of a 3 M potassium hydroxide solution under vigorous stirring. The reaction medium was then heated to 80 °C and stirred mechanically for 30 min. Subsequently, oleic acid (8 mL) was added dropwise, and the mixture was further stirred for another 30 min under the same conditions. The resulting product was collected through magnetic sedimentation and cooled to room temperature. The nanoparticles were then rinsed with ethanol and distilled water to remove excess surfactant. The material was dried in air overnight at 100 °C, then ground into a fine powder and calcined at 400 °C for 1 h.

### 2.3. Synthesis of CoFe<sub>2</sub>O<sub>4</sub>/Cu- or Ce-doped SnO<sub>2</sub> nanocomposite

A sequential hydrothermal and calcination procedure was used to synthesize CoFe<sub>2</sub>O<sub>4</sub>/Cu- or Ce-doped SnO<sub>2</sub> nanocomposites. The CoFe<sub>2</sub>O<sub>4</sub> nanoparticles (100 mg) were combined with varying quantities of Cu- or Ce-doped SnO<sub>2</sub> particles (100, 200 or 300 mg) in absolute ethanol (80 mL) following a general protocol. The resulting mixtures were sonicated for 2 h, maintaining a constant volume of 80 mL by adding absolute ethanol when necessary. Each suspension was then transferred to a Teflon-lined autoclave and heated at 60 °C for 12 h. The resulting precipitates were collected using an external magnet, washed multiple times with distilled water and ethanol, and then dried at 60 °C. Finally, the nanocomposite was formed by annealing the precipitates at 280 °C for 2 h in a muffle furnace, resulting in a strong interaction between the cobalt ferrite and the doped tin oxide.

### 2.4. Material characterization

Several characterizations were performed to analyze the properties of the prepared samples. The microstructure was analyzed using X-ray diffraction (XRD) patterns obtained from a Bruker D8 Advance A 25 X-ray diffractometer equipped with a CuK<sub>α</sub> radiation source (1.54 Å) at 40 kV. To evaluate the morphology of the nanopowders, Scanning Electron Microscopy (SEM) was conducted at 20 kV using FE-SEM JEOL J-7100 instrument. N<sub>2</sub>-physisorption at 77 K with a pressure transducer was used to conduct Brunauer-Emmet-Teller (BET) surface area measurements. The samples were degassed at 100 °C for 12 h under vacuum prior to the N<sub>2</sub> physisorption analyses.

### 2.5. Catalytic experiments

Rhodamine B (Rh-B) degradation and mineralization were assessed at pH 7. Independent experiments were conducted to evaluate the effectiveness of photolytic, sonolytic, sonophotolytic, photocatalytic, sonocatalytic and sonophotocatalytic remediation. A standard procedure was followed, in which 50 mL of a 20 ppm Rh-B solution was subjected to 80 min of illumination using a 1.6 W white LED strip (2.2 × 10<sup>-3</sup> W cm<sup>-2</sup>), sonication with a 40 kHz frequency and 100 W output power, or a combination of both. The experiments used a total catalyst amount of 50 mg. The catalyst was kept in contact with the polluted solution without PMS for 30 min in darkness to establish adsorption-desorption equilibrium. Prior to irradiation, 5 mL of a 2.5 mM PMS solution was added to the reactor. At predefined time intervals ranging from 0 to 80 min, 3 mL samples were extracted, subjected to UV-vis measurements, and subsequently reintroduced into the reaction medium. Degradation and mineralization were quantified using Shimadzu Corporation's UV-1800 UV-vis spectrophotometer and TOC-VCSH equipment, respectively. The TOC content reduction was measured to determine mineralization. The experiments were conducted in triplicate to ensure accuracy. The study evaluated the potential reusability of CoFe<sub>2</sub>O<sub>4</sub>/Cu- and Ce-doped SnO<sub>2</sub> nanocomposite by quantifying the degradation and mineralization of fresh 20 ppm solutions through 15 successive cycles in 80-min sonophotocatalytic experiments. The study investigated the mineralization performance of a multipollutant solution containing 20 ppm of each of rhodamine-B, tetracycline, methylene blue, and levofloxacin under sonophotocatalytic conditions using the two most effective catalysts.

### 2.6. Stability of CoFe<sub>2</sub>O<sub>4</sub>/Cu- or Ce-doped SnO<sub>2</sub> nanocomposites

The stability of CoFe<sub>2</sub>O<sub>4</sub>/Cu- or Ce-doped SnO<sub>2</sub> nanocomposites was assessed by conducting a procedure to determine the impact of exposure to light and ultrasound in the presence of PMS. On the dissolution and release of metallic ions. A 0.23 mM solution of PMS in Milli-Q water (total volume of 50 mL) and pH adjusted to 7, containing 50 mg of the two most effective catalysts, was continuously irradiated with visible

light, facilitated by a 1.6 W white LED strip (2.2 × 10<sup>-3</sup> W cm<sup>-2</sup>) and ultrasound irradiation with a frequency of 40 kHz and an output power of 100 W for 24 h. In the sonophotocorrosion experiments, we performed multiple short cycles over a total duration of 24 h to prevent a significant temperature rise. After, the solution was subjected to centrifugation, adjusted to the initial 50 mL with Milli-Q water, and then filtered through a 0.22 μm syringe filter to determine the concentrations of iron, cobalt, tin, copper, and cerium ions. The concentration of metallic ions in solution was measured using inductively coupled plasma-mass spectrometry (ICP-MS).

## 3. Results and discussion

### 3.1. Characterization of Cu- and Ce-doped SnO<sub>2</sub> nanoparticles

Fig. 1a–b shows the X-ray diffraction spectra of pure SnO<sub>2</sub>, Ce-doped SnO<sub>2</sub> and Cu-doped SnO<sub>2</sub> nanopowders heat-treated at 500 °C for 2 h in air. The undoped SnO<sub>2</sub> material exhibited diffraction peaks at 2θ values of 26.61°, 34.11°, 37.94°, 52.03°, 54.58°, 58.29°, 61.84°, 65.68°, 71.50° and 79.04°, which are related to (110), (101), (111), (211), (220), (002), (310), (202), (320), and (321) planes, respectively. The peaks observed in the synthesized materials indicate a tetragonal rutile geometry, which is in accordance with the standard diffraction card N° 41-1445 (Babu et al., 2017). These same peaks were also observed in the Ce-doped and Cu-doped spectra. The absence of secondary phases, such as CeO<sub>2</sub> or CuO, in the patterns indicates the purity of the synthesized samples and the successful incorporation of Ce and Cu ions into the SnO<sub>2</sub> network. The sample doped with 3 at.% Ce exhibited broader peaks, indicating that Ce atoms limited the growth of larger crystallites, which is consistent with prior research (Liu et al., 2012; Weber et al., 2004). The peaks recorded from the Cu-doped samples were more intense than those in pure and Ce-doped samples. The average crystallite sizes, determined using Scherrer's formula, were 5 nm for SnO<sub>2</sub>, 7 nm for SnO<sub>2</sub>:Ce<sub>1%</sub>, 4 nm for SnO<sub>2</sub>:Ce<sub>3%</sub>, and 6 nm for SnO<sub>2</sub>:Ce<sub>5%</sub>. In contrast, the average crystallite sizes of the Cu-doped SnO<sub>2</sub> samples are as follows: 8 nm for SnO<sub>2</sub>:Cu<sub>1%</sub>, 6 nm for SnO<sub>2</sub>:Cu<sub>3%</sub>, and 9 nm for SnO<sub>2</sub>:Cu<sub>5%</sub>.

The FE-SEM images presented in Fig. 1c–h depict the morphology and dimensions of undoped SnO<sub>2</sub> and SnO<sub>2</sub> doped with Ce or Cu. The undoped SnO<sub>2</sub> particles were observed to have diverse shapes and sizes, with an approximate diameter of 1 μm. The introduction of cerium caused alterations in grain size and shape. Specifically, the 1 at. % and 3 at. % Ce-doped samples exhibited regular and spherical grains measuring 1–2 μm, in contrast to the pure sample. The samples with a Ce concentration of 5 at. % exhibited an agglomeration phenomenon, resulting in larger irregularly-shaped ones. The sample with 1 at. % Cu also displayed irregularly-shaped grains of varying sizes. However, with an increased Cu concentration of 3 at. %, the grains became spherical and some agglomerates formed. In the sample with 5 at. %, a larger number of agglomerates were observed, leading to an increase in grain size and changes in grain shape.

Another important factor in heterogeneous catalytic processes is the active and accessible surface area of the catalyst. The surface area values were consistent with the FE-SEM images, with non-doped tin oxide having a surface area of 76 m<sup>2</sup>g<sup>-1</sup>. The effect of the dopant on the surface area depends on the amount and chemical nature. Doping with 1 at. % Ce resulted in a slight increase to 82 m<sup>2</sup>g<sup>-1</sup>, while doping with 3 at. % Ce or 1 at.% Cu resulted in surface areas of 80 m<sup>2</sup>g<sup>-1</sup> and 84 m<sup>2</sup>g<sup>-1</sup>, respectively. For Ce at. 5% (58 m<sup>2</sup>g<sup>-1</sup>), Cu at. 3% (67 m<sup>2</sup>g<sup>-1</sup>), or Cu at 5% (61 m<sup>2</sup>g<sup>-1</sup>), the reduction in area was more significant due to the formation of aggregates and variations in entity size.

### 3.2. Characterization of CoFe<sub>2</sub>O<sub>4</sub> nanoparticles

The FE-SEM and X-ray diffraction techniques were used to survey the morphological and structural characteristics of the CoFe<sub>2</sub>O<sub>4</sub> nanoparticles, as shown in Fig. 2. The nanoparticles exhibited a wide range of

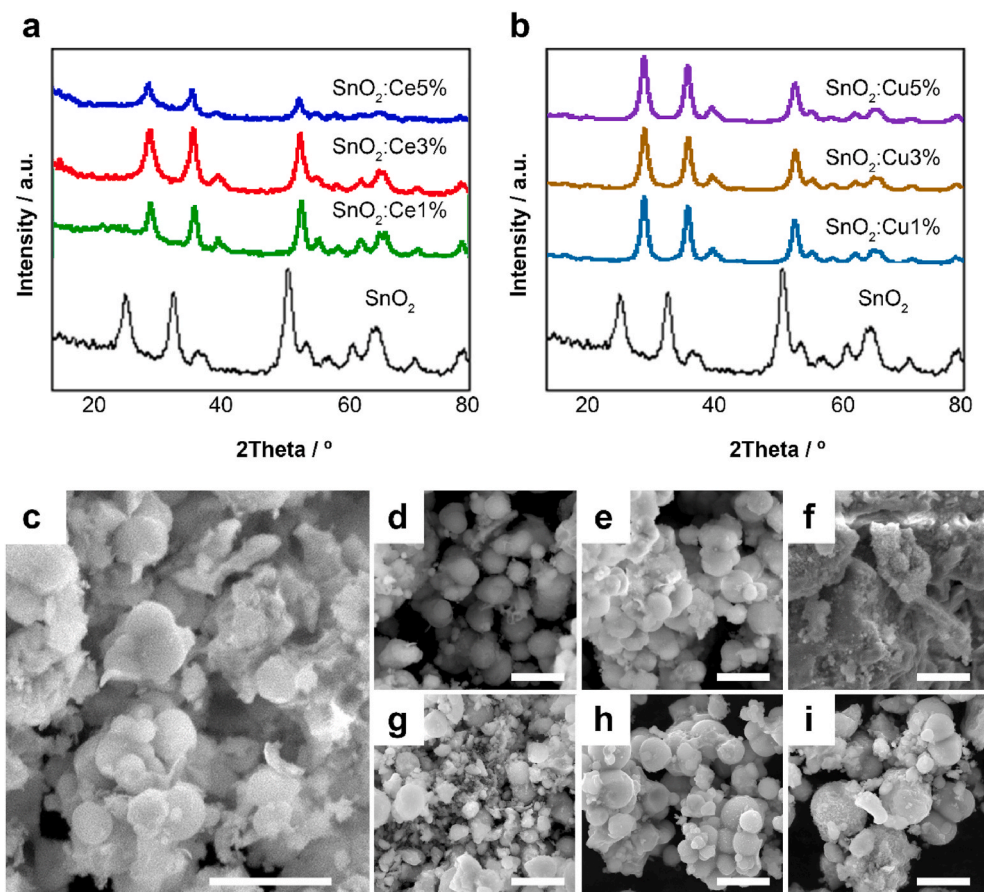


**Fig. 1.** XRD patterns of (a) Ce-doped SnO<sub>2</sub> and (b) Cu-doped SnO<sub>2</sub> nanomaterials. FE-SEM micrographs of (c) SnO<sub>2</sub>, (d) SnO<sub>2</sub>:Ce<sub>1%</sub>, (e) SnO<sub>2</sub>:Ce<sub>3%</sub>, (f) SnO<sub>2</sub>:Ce<sub>5%</sub>, (g) SnO<sub>2</sub>:Cu<sub>1%</sub>, (h) SnO<sub>2</sub>:Cu<sub>3%</sub>, and (i) SnO<sub>2</sub>:Cu<sub>5%</sub>. Scale bar: 5 μm.

sizes within the nanoscale, ranging from a few to hundreds of nanometers, with most of them having a spherical shape. The larger grains and domains detected were attributed to agglomeration caused by their non-dispersive nature. Fig. 2a presents three representative FE-SEM images, while Fig. 2b shows the X-ray diffraction spectra of the prepared cobalt ferrite nanoparticles. The material exhibited diffraction peaks at  $2\theta$  values of 18.28°, 30.08°, 35.43°, 37.05°, 43.03°, 56.97°, and 62.58°, related to (111), (220), (311), (222), (400), (511), and (440) planes, respectively. The peaks observed correspond to the characteristic peaks of a spinel structure of CoFe<sub>2</sub>O<sub>4</sub>, as per standard diffraction card N° 22–1086 (Basak et al., 2022). Additionally, the agreement between the pattern and the card suggests the absence of impurities in the sample, such as iron oxides. The BET surface area of cobalt ferrite nanoparticles was around 135 m<sup>2</sup>g<sup>-1</sup>.

### 3.3. Photolytic, sonolytic and sonophotolytic degradation of Rh-B

Fig. 3 shows the impact of visible light, ultrasound, and their simultaneous application over an 80-min duration on two separate solutions of Rh-B at 20 ppm and pH = 7, with and without the presence of PMS (0.23 mM). The results indicate that light exposure had minimal effects in both scenarios, resulting in degradation levels of approximately 1% without PMS and 3% with PMS. Mineralization of contaminants remained minimal in these cases. In contrast, application of ultrasound resulted in significantly different outcomes. In the absence of PMS, a degradation rate of 7% was achieved, while in its presence, degradation levels reached 28%. Similarly, the absence of PMS resulted in a TOC reduction of 2%, whereas its presence led to a mineralization of 11%. These variations can be attributed to the extreme conditions generated during the cavitation process, which facilitate the cleavage of

the O–O bond (Xu et al., 2020). In the case of sonophotolysis, the results closely mirrored those obtained with ultrasound alone. Degradation levels of 9% and 33% were observed, with mineralizations of 5% and 12% in the absence and presence of PMS, respectively.

### 3.4. Photocatalytic, sonocatalytic and sonophotocatalytic degradation of Rh-B via Cu- or Ce-doped SnO<sub>2</sub> particles or CoFe<sub>2</sub>O<sub>4</sub> nanoparticles

The study evaluated the impact of light, ultrasound, and their concurrent application in the presence of catalysts on the degradation and mineralization of Rh-B, both with and without the presence of PMS (0.23 mM). Various tin oxides doped with Cu and Ce or cobalt ferrite were used as catalysts to identify the most suitable materials for composite preparation. The results of the study indicate that SnO<sub>2</sub>:Cu<sub>3%</sub> and SnO<sub>2</sub>:Ce<sub>1%</sub> photocatalysts achieved the most favorable degradation and mineralization rates under visible light in the absence of PMS. Specifically, degradation rates of 78% and 83%, respectively, were achieved, as well as mineralizations of 34% and 38%, respectively (Fig. 4a and d). In contrast, the undoped catalyst exhibited modest degradation (44%) and mineralization (22%). Cu doping significantly enhanced photocatalytic activity, with the highest efficiency observed for SnO<sub>2</sub>:Cu<sub>3%</sub>. However, Ce doping showed substantial photocatalytic improvement at a 1% percentage but led to reduced degradation and mineralization at higher Ce levels, likely due to the size of final particles. Cobalt ferrite exhibited low efficiency, resulting in only 6% degradation and 3% mineralization.

In the presence of PMS (as shown in Fig. 4a and d), the SnO<sub>2</sub>-based photocatalysts exhibited similar trends but with significantly enhanced catalytic activities. Notably, the SnO<sub>2</sub>:Cu<sub>3%</sub> and SnO<sub>2</sub>:Ce<sub>1%</sub> samples achieved degradation levels of 89% and 94%, respectively, with

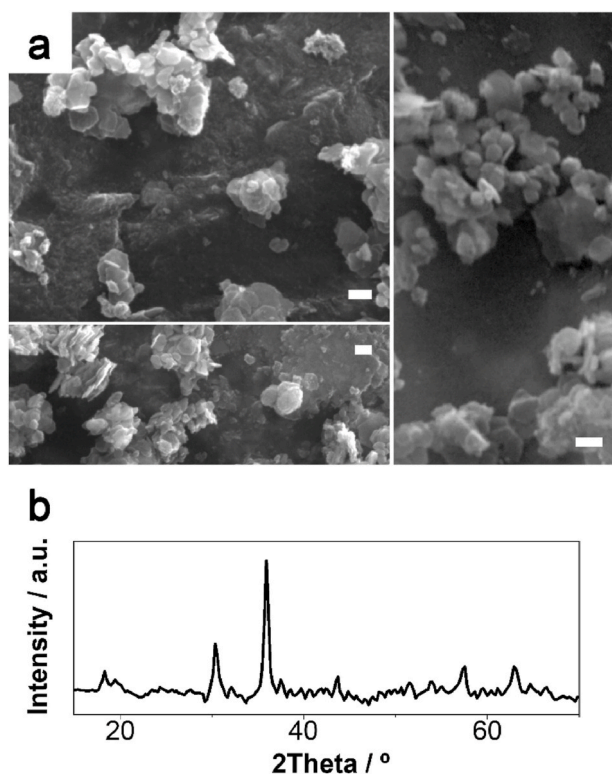


Fig. 2. (a) FE-SEM micrographs and (b) XRD patterns of  $\text{CoFe}_2\text{O}_4$  nanoparticles. Scale bar: 80 nm.

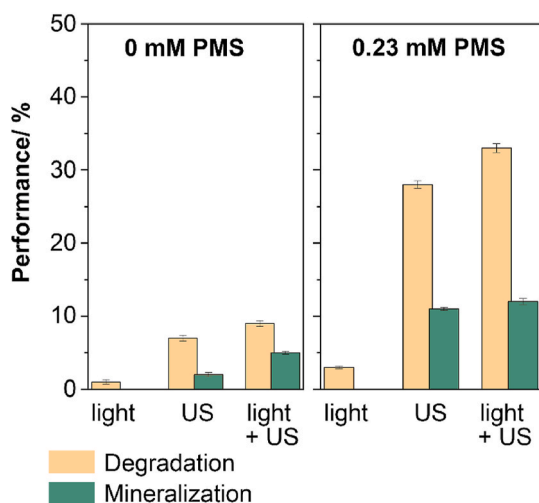


Fig. 3. Rh-B degradation and mineralization after 80 min of visible light irradiation, ultrasound irradiation, or their simultaneous application. Experimental parameters: Initial rhodamine-B concentration of 20 ppm,  $[\text{PMS}] = 0.0$  or 0.23 mM, temperature maintained at 20 °C, and pH adjusted to 7.0.

corresponding mineralizations of 40% and 43%. It is important to highlight that the degradation efficiency of cobalt ferrite significantly increased in the presence of PMS, reaching degradation values of 88% and approximately 40% mineralization. The superior performance of cobalt ferrite was attributed more to its chemical nature than to light exposure. Similar results were obtained in the absence of light. XRD and FE-SEM analyses indicated little difference in the crystallite size and shape of nanoparticles in the undoped and doped samples with different Cu and Ce concentrations. Therefore, we can exclude an increase in surface area as the main cause of the observed enhancement in

degradation level observed on doped  $\text{SnO}_2$  catalysts. The high degradation can be explained as follows: appropriate quantities of copper and cerium can capture photoinduced electrons, which increases the number of hydroxyl radicals and shifts the absorption wavelength to the visible. Increasing the amount of doping resulted in a decrease in rhodamine B degradation likely due to a reduction of active sites.

Comparable degradation and mineralization values were observed across various catalysts for sonocatalytic activity in the dark without PMS. It is important to note that all evaluations presented are objective and free from bias (Fig. 4b and e). The differences in efficiency were primarily attributed to particle size rather than composition. Cobalt ferrite achieved higher efficiency due to its smaller particle size, with degradation of 64% and mineralization of 29%. In the presence of PMS, the tin oxide catalysts exhibited higher rates of degradation and mineralization compared to when PMS was absent. Degradation rates ranged from 72% to 76%, with mineralization rates ranging from 36% to 42%. Cobalt ferrite achieved 96% degradation and 42% mineralization.

Fig. 4c and f presents degradation and mineralization data when light and ultrasound were simultaneously applied. The results show that  $\text{SnO}_2:\text{Cu}_{3\%}$  and  $\text{SnO}_2:\text{Ce}_{1\%}$  photocatalysts achieved enhanced degradation, indicating the synergistic effect of sonophotocatalysis. These catalysts achieved degradations of 89% and 94%, with corresponding mineralizations of 43% and 44%. The trends observed for other catalysts were consistent with previous photocatalysis and sonocatalysis results. Cobalt ferrite exhibited similar performance to sonocatalysis, achieving 92% degradation and 43% mineralization. In the presence of PMS,  $\text{SnO}_2:\text{Cu}_{3\%}$ ,  $\text{SnO}_2:\text{Ce}_{1\%}$ , and  $\text{CoFe}_2\text{O}_4$  were the top options, achieving degradation rates of approximately 99%, 99%, and 96%, respectively, along with mineralizations of 64%, 66%, and 57%. Based on these findings, the combination of either  $\text{SnO}_2:\text{Cu}_{3\%}$  or  $\text{SnO}_2:\text{Ce}_{1\%}$  with  $\text{CoFe}_2\text{O}_4$  for the synthesis of nanocomposites was the recommended next step.

### 3.5. Synthesis and characterization of $\text{CoFe}_2\text{O}_4/\text{Cu}$ - and $\text{Ce}$ -doped $\text{SnO}_2$ nanocomposites

The  $\text{CoFe}_2\text{O}_4/\text{Cu}$ - and  $\text{Ce}$ -doped  $\text{SnO}_2$  nanocomposites were prepared by combining the  $\text{CoFe}_2\text{O}_4$  nanoparticles with  $\text{SnO}_2:\text{Cu}_{3\%}$  or  $\text{SnO}_2:\text{Ce}_{1\%}$  in different ratios (1:1, 1:2 and 1:3  $\text{CoFe}_2\text{O}_4$ :doped  $\text{SnO}_2$  wt%). Fig. 5 shows the FE-SEM and X-ray diffraction patterns of the resulting six composites.

The morphology of the  $\text{CoFe}_2\text{O}_4$  nanoparticles, as characterized in section 3.2., can be observed throughout the surface of some of the composites, indicating their adhesion to the micrometric Cu- and Ce-doped  $\text{SnO}_2$  substrates. This morphology was visible for the 1:1 and 1:2 ratios of  $\text{CoFe}_2\text{O}_4/\text{Cu}$ -doped  $\text{SnO}_2$  (Fig. 5a and b). For the Ce-doped analogs, the 1:2 ratio was the most representative (Fig. 5f). In contrast, a ratio of 1:3 of  $\text{CoFe}_2\text{O}_4$  to Cu- or Ce-doped  $\text{SnO}_2$  (as shown in Fig. 5c and g) resulted in a less-texturized and more uniform material. This could indicate a higher degree of blending between the materials due to an unbalanced ratio of  $\text{SnO}_2$ . This effect is particularly noticeable in the case of the Ce-doped  $\text{SnO}_2$ . Additionally, the elemental map of Fe and Sn indicated a uniform distribution in all samples, confirming the formation of the nanocomposites. A uniform distribution of the composite's constituent entities was essential to ensure its integrity and the durability of its catalytic activity.

The X-ray diffraction patterns in Fig. 5d and h indicate that all six samples maintain the structure of their original components, specifically the spinel packing of  $\text{CoFe}_2\text{O}_4$  and tetragonal rutile geometry of  $\text{SnO}_2$ . The presence of impurities can also be ruled out, further supporting the successful synthesis of the composites.

The BET surface area of the nanocomposites depended on the relative amount of each component. Specifically, when the relative amount of cobalt ferrite was greater, the surface area was also greater. The obtained BET surfaces were 99 (1:1  $\text{CoFe}_2\text{O}_4/\text{Cu}$ -doped  $\text{SnO}_2$ ), 95 (1:2  $\text{CoFe}_2\text{O}_4/\text{Cu}$ -doped  $\text{SnO}_2$ ), 88 (1:3  $\text{CoFe}_2\text{O}_4/\text{Cu}$ -doped  $\text{SnO}_2$ ), 102 (1:1  $\text{CoFe}_2\text{O}_4/\text{Ce}$ -doped  $\text{SnO}_2$ ), 94 (1:2  $\text{CoFe}_2\text{O}_4/\text{Ce}$ -doped  $\text{SnO}_2$ ), and 92

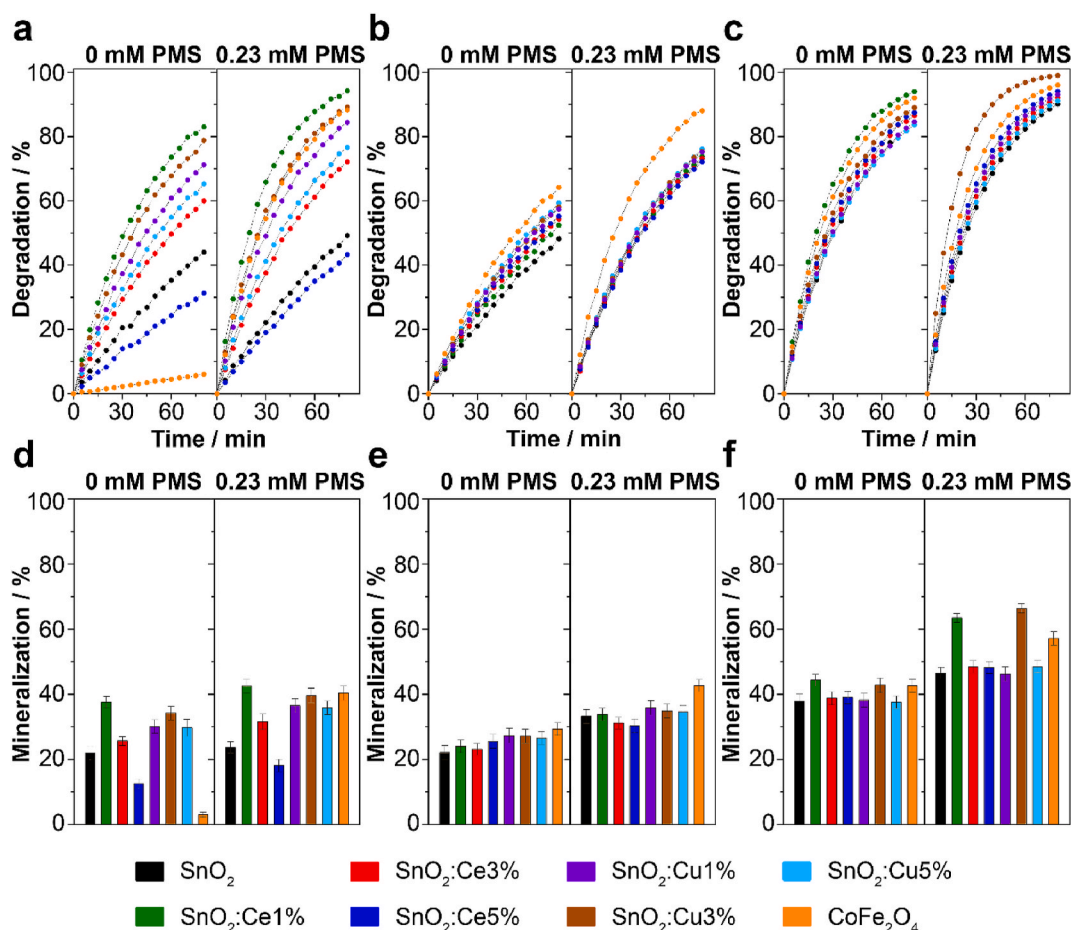


**Fig. 4.** Rhodamine-B Degradation (a, b, and c) and mineralization (d, e, and f) using various catalysts (SnO<sub>2</sub>, SnO<sub>2</sub>:Ce1%, SnO<sub>2</sub>:Ce3%, SnO<sub>2</sub>:Ce5%, SnO<sub>2</sub>:Cu1%, SnO<sub>2</sub>:Cu3%, SnO<sub>2</sub>:Cu5%, and CoFe<sub>2</sub>O<sub>4</sub>) under different irradiation conditions: (a and d) visible light, (b and e) ultrasound, and (c and f) simultaneous visible light and ultrasound treatment. Light conditions: visible light with an irradiance of  $2.2 \times 10^{-3} \text{ W cm}^{-2}$ ; Ultrasound conditions: 40 kHz frequency and 100 W output power. Experimental parameters: Initial rhodamine-B concentration of 20 ppm, [PMS] = 0.23 mM, catalyst dosage = 1 mg mL<sup>-1</sup>, temperature maintained at 20 °C, and pH adjusted to 7.0.

(1:3 CoFe<sub>2</sub>O<sub>4</sub>/Ce-doped SnO<sub>2</sub>) m<sup>2</sup>g<sup>-1</sup>, which are quite comparable between ratios.

### 3.6. Sonophotocatalytic degradation and mineralization activity of CoFe<sub>2</sub>O<sub>4</sub>/Cu- and Ce-doped SnO<sub>2</sub> nanocomposites

The sonophotocatalytic activity for both the degradation and mineralization of Rh-B is significantly enhanced by the synergistic interaction between SnO<sub>2</sub> particles doped with Cu or Ce and CoFe<sub>2</sub>O<sub>4</sub> nanoparticles, which leads to the formation of a heterojunction. This improved sonophotocatalytic efficiency is attributed to the facilitation of photogenerated charge separation.

For CoFe<sub>2</sub>O<sub>4</sub>/Cu-doped SnO<sub>2</sub>, it is important to note that the degradation process was exceptionally rapid when a 1:1 ratio composite was used, achieving degradation rates close to 100% in less than 5 min (Fig. 6a). Therefore, the values obtained with the combination of CoFe<sub>2</sub>O<sub>4</sub> and Cu-doped SnO<sub>2</sub> surpassed those obtained with either material alone. This was observed regardless of the treatment applied, as none of the materials achieved 100% degradation rates even after 80 min of simultaneous ultrasound and light irradiation. The formation of heterojunctions, which enhances the efficiency of photogenerated charge separation, is believed to be responsible for this phenomenon. The sonophotocatalytic activation of PMS generates multiple active species, including •OH, O<sub>2</sub>•<sup>-</sup>, SO<sub>4</sub>•<sup>-</sup>, and <sup>1</sup>O<sub>2</sub>, contributing to the degradation of organic matter. Mineralization showed a similar trend, with greater significance during the initial reaction times. The CoFe<sub>2</sub>O<sub>4</sub>/

Cu-doped SnO<sub>2</sub> (1:1) nanocomposite achieved over 70% mineralization in just 5 min, increasing to around 90% after 80 min (Fig. 6b). Total mineralization required more extended times, being approximately 100% after 180 min.

The study found that the CoFe<sub>2</sub>O<sub>4</sub>/Ce-doped SnO<sub>2</sub> (1:2) nanocomposite was the most effective material for nanocomposite with SnO<sub>2</sub> particles doped with Ce. This nanocomposite exhibited degradation (Fig. 6a) and mineralization (Fig. 6b) results similar to those achieved with the CoFe<sub>2</sub>O<sub>4</sub>/Cu-doped SnO<sub>2</sub> (1:1) nanocomposite. There was no significant difference observed between these two composite types. The results are competitive and comparable to the state-of-the-art materials and strategies for mineralizing organic pollutants through heterogeneous catalytic PMS activation as demonstrated by previous studies (Table S1) (Bein et al., 2023; Du et al., 2016; Giannakis et al., 2021; R. R. Guo et al., 2020; S. S. Guo et al., 2020; Ren et al., 2018; M. W. Wang et al., 2023; Xu et al., 2019; Yang et al., 2018; Ye et al., 2020).

It is noteworthy that the surface of the photocatalyst in composites containing Cu-doped SnO<sub>2</sub> was more accessible than in the case of Ce-doped SnO<sub>2</sub>, as shown in Fig. 5. This increased accessibility allowed for an increase in quantity of cobalt ferrite. It is also important to ensure that the composite has sufficient magnetic character to facilitate its collection and recovery, while preventing magnetic agglomeration of the composites. The agglomeration of the nanocomposites could potentially reduce the catalytic activity of the system. However, we were able to achieve a 1:1 ratio by effectively suspending the nanocomposites in the reaction medium with the aid of ultrasound.

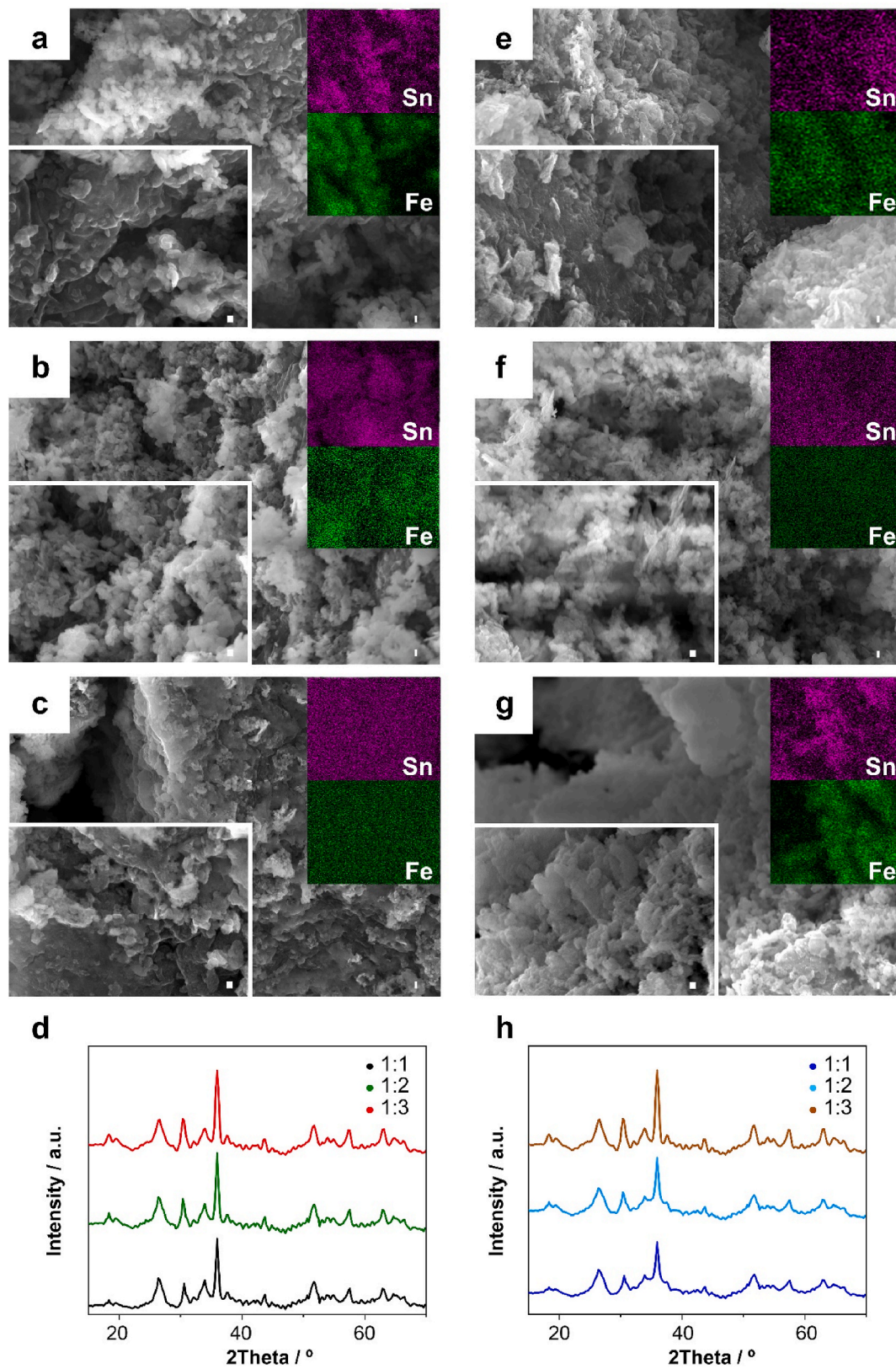


**Fig. 5.** FE-SEM micrographs of (a) 1:1, (b) 1:2, and (c) 1:3 CoFe<sub>2</sub>O<sub>4</sub>/Cu-doped SnO<sub>2</sub> and (e) 1:1, (f) 1:2, and (g) 1:3 CoFe<sub>2</sub>O<sub>4</sub>/Ce-doped SnO<sub>2</sub> nanocomposites (EDS maps of Fe and Sn are also included). Scale bar: 80 nm. XRD patterns of (d) CoFe<sub>2</sub>O<sub>4</sub>/Cu-doped SnO<sub>2</sub> and (h) CoFe<sub>2</sub>O<sub>4</sub>/Ce-doped SnO<sub>2</sub> nanocomposites.

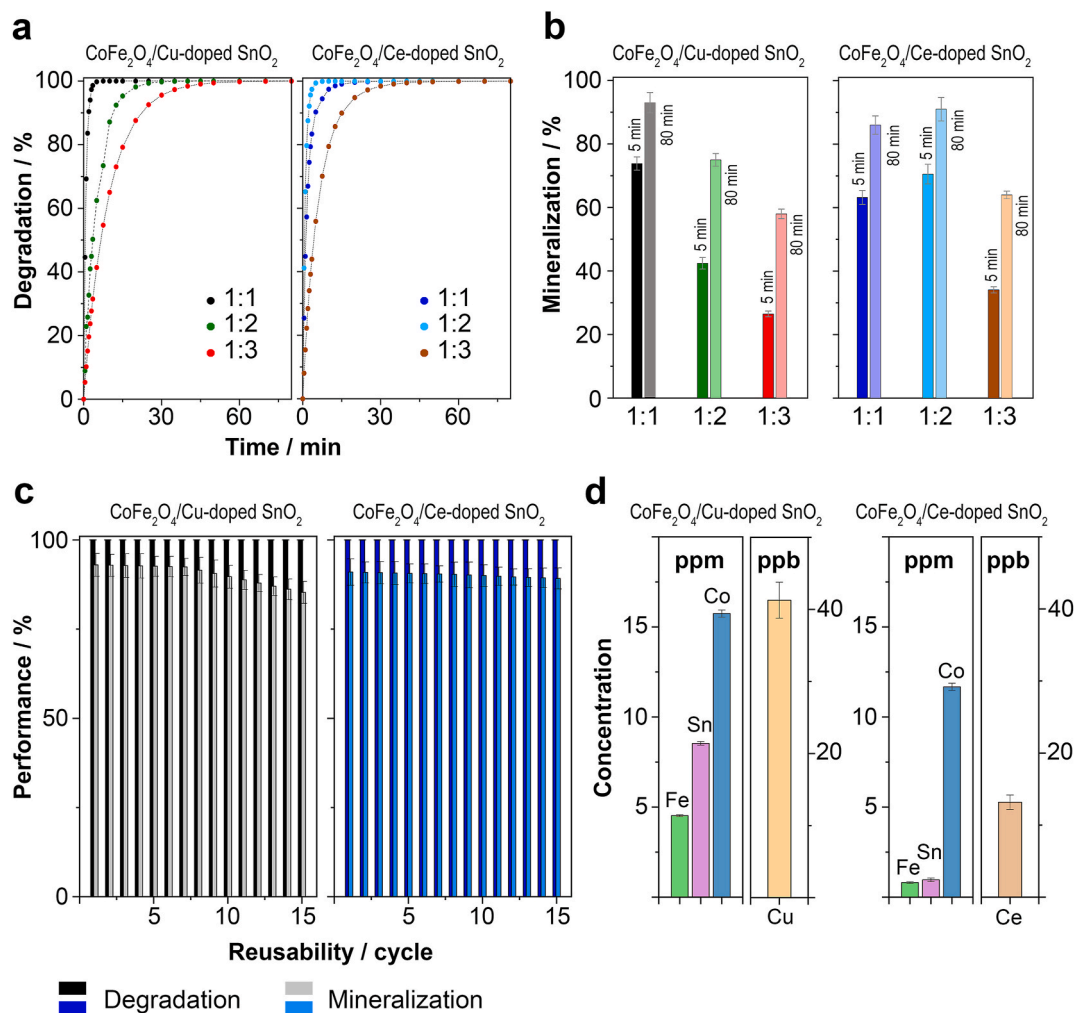


**Fig. 6.** (a) Degradation and (b) mineralization of rhodamine-B using CoFe<sub>2</sub>O<sub>4</sub>/Cu- or Ce-doped SnO<sub>2</sub> nanocomposites in a sonophotocatalytic system (Light conditions: visible light with an irradiance of  $2.2 \times 10^{-3} \text{ W cm}^{-2}$ ; Ultrasound conditions: 40 kHz frequency and 100 W output power). (a and b) Experimental conditions: Initial Rhodamine-B concentration of 20 ppm, [PMS] = 0.23 mM, catalyst dosage = 1 mg mL<sup>-1</sup>, temperature maintained at 20 °C, and pH adjusted to 7.0. (c) Reusability of CoFe<sub>2</sub>O<sub>4</sub>/Cu-doped SnO<sub>2</sub> (1:1) and CoFe<sub>2</sub>O<sub>4</sub>/Ce-doped SnO<sub>2</sub> (1:2) nanocomposites over 15 consecutive 80-min cycles for degrading and mineralizing Rh-B under sonophotocatalytic conditions (Light conditions: visible light with irradiance of  $2.2 \times 10^{-3} \text{ W cm}^{-2}$ ; Ultrasound conditions: 40 kHz frequency and 100 W output power). Experimental conditions: Initial Rhodamine-B concentration of 20 ppm, [PMS] = 0.23 mM, catalyst dosage = 1 mg mL<sup>-1</sup>, temperature maintained at 20 °C, and pH adjusted to 7.0. (d) Concentration of Fe, Sn, Co and Cu or Ce ions in solution after 24 h of using CoFe<sub>2</sub>O<sub>4</sub>/Cu-doped SnO<sub>2</sub> (1:1) and CoFe<sub>2</sub>O<sub>4</sub>/Cu-doped SnO<sub>2</sub> (1:2) nanocomposites under ultrasound and light irradiation conditions. (c and d) Experimental conditions: Initial Rhodamine-B concentration of 0 ppm, [PMS] = 0.23 mM, catalyst dosage = 1 mg mL<sup>-1</sup>, and pH adjusted to 7.0.

When evaluating a catalyst's potential for water treatment applications, it is important to consider its reusability without the need for extensive recovery treatments, as well as its long-term chemical stability and sonophotochemical performance. To assess these factors, the capability of the catalyst to degrade and mineralize successive 20 ppm Rh-B solutions was examined. Fig. 6c shows the degradation and mineralization rates of both composites. In both cases, the degradation remained nearly constant through reusability cycles, achieving approximately 100% of Rh-B degradation. However, a slight reduction in the mineralization rate was observed from the seventh cycle for the CoFe<sub>2</sub>O<sub>4</sub>/Cu-doped SnO<sub>2</sub> (1:1) nanocomposite.

In contrast, the CoFe<sub>2</sub>O<sub>4</sub>/Ce-doped SnO<sub>2</sub> (1:2) nanocomposite showed consistent mineralization with only a slight reduction. After 15 cycles, applying a heat treatment at 250 °C for 2 h to either composite resulted in mineralization values almost identical to those of the original composites. The magnetic properties of cobalt ferrite are particularly useful in catalyst recovery, making it easier to reuse and collect. However, 1:3 ratios exhibit low magnetic properties, making magnetic collection challenging.

In terms of chemical stability, both compounds remained stable in an aqueous medium for up to 8 days when kept in the dark. It is worth noting that no traces of Fe, Co, Sn, Cu, or Ce were detected in the aqueous medium. Under operational conditions, both composites exhibited a catalyst dissolution of less than 2% over a 24-h period in the absence of organic matter, with both compounds present at a concentration of 1 mg mL<sup>-1</sup> (Fig. 6d). The CoFe<sub>2</sub>O<sub>4</sub>/Ce-doped SnO<sub>2</sub> (1:2) catalyst experienced slightly less sonophotocorrosion when compared to the other composite. Based on these findings, it can be concluded that both composites have the potential for application in the sonophotocatalytic activation of PMS and subsequent mineralization of organic contaminants. Catalyst dissolution may impact the catalytic process of PMS activation, as certain metal ions can act as homogeneous catalysts for PMS activation. However, it is important to note that the amount of metallic ions released during each cycle in the presence of organic pollutants cannot be detected. The values presented in Fig. 6d were obtained after 24 h of irradiation with light and ultrasound, but in the absence of contaminants. It is worth highlighting the behavior observed when the reaction medium contains organic matter, conditions in which

the corrosion of the catalysts is significantly reduced. The study evaluated the effect of 1 ppm of Co, Sn, Fe, Cu, or Ce ions. In all cases, a slight activation was detected, particularly in the case of Fe and Cu ions. However, this increase represented less than 8% of the rate of degradation and mineralization obtained in the absence of a heterogeneous catalyst. Therefore, the main contribution is due to the heterogeneous PMS activation driven by our catalysts.

The evaluation focused on the mineralization of a multi-contaminated solution containing antibiotics and dyes, with an initial concentration of approximately 80 ppm (Fig. 7). After 80 min, the achieved values were close to, but slightly lower than, those obtained when dealing with a single solution contaminated with 20 ppm of Rh-B. The oxidation of organic matter through highly reactive radical species lacks selectivity. This observation indicates that the catalyst's surface contains active centers of different natures, capable of facilitating the adsorption of various organic compounds and promote the degradation and subsequent oxidation. It is important to note that the contaminants are mainly adsorbed on the catalyst surfaces or at the solid-liquid interface, where the formation rate of radical species is highest. This is significant because these materials allow for the simultaneous oxidation of organic compounds with different chemical structures and properties. This is highly advantageous for treating complex matrices that may contain numerous organic contaminants. Extending the reaction time allows for the complete mineralization of organic matter.

#### 4. Conclusions

This study surveyed a set of materials based on cobalt ferrite and tin oxide, whether pristine or Cu- or Ce-doped, as catalysts for the degradation and mineralization of an organic compound under different conditions, as test pollutant Rhodamine B was used. The presence of PMS was found to enhance the performance of the process, which was especially notable in the case of  $\text{CoFe}_2\text{O}_4$ . Exposure to light or ultrasound treatment can improve the degradation and mineralization rates, with the best results achieved through a sonophotocatalytic combination. Cu3%- and Ce1%-doped  $\text{SnO}_2$  outperformed other doped  $\text{SnO}_2$  catalysts under these conditions, while the activity of  $\text{CoFe}_2\text{O}_4$  was noteworthy. As a result, six different nanocomposites were created by combining the promising features of  $\text{CoFe}_2\text{O}_4$  and Cu- or Ce-doped  $\text{SnO}_2$ , with variations in terms of wt%. The study investigated the sonophotocatalytic degradation of rhodamine B using a mixture of doping metal and a specific ratio. XRD and FE-SEM were used to characterize the prepared materials, which showed no impurities and adequate morphology. The nanocomposites used in the sonophotocatalytic experiments resulted in increased degradation and mineralization rates of the pollutant. The optimized compositions,  $\text{CoFe}_2\text{O}_4/\text{Cu}3\%$ -doped  $\text{SnO}_2$  (1:1) and Ce1%-doped  $\text{SnO}_2$  (1:2), achieved complete degradation and mineralization exceeding 70% in just 5 min. Therefore, a precise balance of the mixture ratio, rather than the type of doping metal, resulted in a promising material. Additionally, the dual  $\text{CoFe}_2\text{O}_4/\text{doped SnO}_2$  composition effectively addressed the poor reusability and instability that often plagues some cobalt-based nanostructures. The metal traces released into the medium were minimal, even under harsh conditions, such as in the absence of pollutants. Ce doping was found to be slightly superior for long-term usage, as demonstrated by the reusability after 15 cycles. The versatility of these traces was also notable, as they were able to effectively treat a heterogeneous mixture of pollutants. Overall, these nanocomposites exhibit superior sonophotocatalytic performance compared to previously reported materials, demonstrating the potential of this non-sophisticated approach.

#### CRedit authorship contribution statement

**Mokhtar Hjiri:** Writing – original draft, Project administration, Methodology, Investigation. **Roger Bujaldón:** Writing – original draft, Visualization, Validation, Project administration, Methodology,

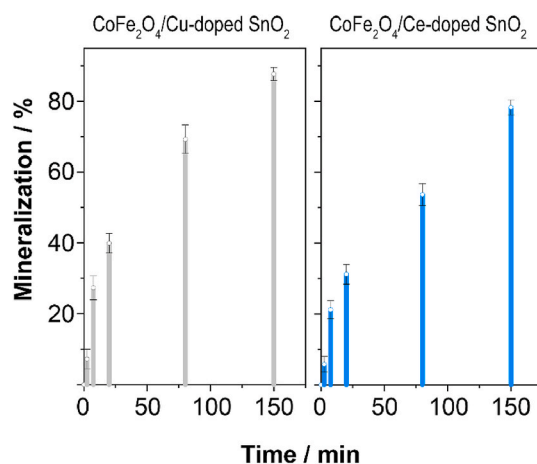


**Fig. 7.** Mineralization of a multipollutant solution containing 20 ppm of rhodamine-B, 20 ppm of tetracycline, 20 ppm of methylene blue, and 20 ppm of levofloxacin under sonophotocatalytic conditions using  $\text{CoFe}_2\text{O}_4/\text{Cu}$ -doped  $\text{SnO}_2$  (1:1) and  $\text{CoFe}_2\text{O}_4/\text{Ce}$ -doped  $\text{SnO}_2$  (1:2) nanocomposites (Light conditions: visible light with an irradiance of  $2.2 \times 10^{-3} \text{ W cm}^{-2}$ , Ultrasound conditions: 40 kHz frequency and 100 W output power). Experimental conditions: [PMS] = 0.23 mM, catalyst dosage =  $1 \text{ mg mL}^{-1}$ , temperature maintained at  $20^\circ\text{C}$ , and pH adjusted to 7.0. (For interpretation of the references to colour in this figure legend, the reader is referred to the Web version of this article.)

Investigation, Data curation. **Judit Lloreda:** Writing – original draft, Methodology, Investigation, Data curation. **Elvira Gómez:** Writing – review & editing, Writing – original draft, Visualization, Resources, Project administration, Formal analysis, Conceptualization. **Albert Serrà:** Writing – review & editing, Writing – original draft, Visualization, Validation, Supervision, Project administration, Investigation, Funding acquisition, Formal analysis, Conceptualization.

#### Declaration of competing interest

Authors declare no conflict of interest.

#### Data availability

Data will be made available on request.

#### Acknowledgements

Grant PID2020-115663 GB-C32 funded by MCIN/AEI/10.13039/501100011033. Authors thank the CCI-T-UB for the use of their equipment.

#### Appendix A. Supplementary data

Supplementary data to this article can be found online at <https://doi.org/10.1016/j.chemosphere.2024.141656>.

#### References

- Babu, B., Kadam, A.N., Ravikumar, R.V.S.S.N., Byon, C., 2017. Enhanced visible light photocatalytic activity of Cu-doped  $\text{SnO}_2$  quantum dots by solution combustion synthesis. *J. Alloys Compd.* 703, 330–336. <https://doi.org/10.1016/j.jallcom.2017.01.311>.
- Barzegar, G., Jorfi, S., Zarezade, V., Khatebasreh, M., Mehdipour, F., Ghanbari, F., 2018. 4-Chlorophenol degradation using ultrasound/peroxymonosulfate/nanoscale zero valent iron: reusability, identification of degradation intermediates and potential application for real wastewater. *Chemosphere* 201, 370–379. <https://doi.org/10.1016/j.chemosphere.2018.02.143>.
- Basak, M., Rahman, M.L., Ahmed, M.F., Biswas, B., Sharmin, N., 2022. The use of X-ray diffraction peak profile analysis to determine the structural parameters of cobalt ferrite nanoparticles using Debye-Scherrer, Williamson-Hall, Halder-Wagner and

- Size-strain plot: different precipitating agent approach. *J. Alloys Compd.* 895, 162694 <https://doi.org/10.1016/j.jallcom.2021.162694>.
- Bein, E., Yechezkel, Y., Zucker, I., Drewes, J.E., Hübner, U., 2023. A novel catalytic filtration process using MnO<sub>2</sub>@sand and peroxymonosulfate for unselective removal of organic contaminants from water. *Chem. Eng. J.* 476 <https://doi.org/10.1016/j.cej.2023.146636>.
- Bembibre, A., Benamara, M., Hjiri, M., Gómez, E., Alamri, H.R., Dhahri, R., Serrà, A., 2022. Visible-light driven sonophotocatalytic removal of tetracycline using Cd-doped ZnO nanoparticles. *Chem. Eng. J.* 427 <https://doi.org/10.1016/j.cej.2021.132006>.
- Brillas, E., Garcia-Segura, S., 2023. Recent progress of applied TiO<sub>2</sub> photoelectrocatalysis for the degradation of organic pollutants in wastewaters. *J. Environ. Chem. Eng.* 11, 109635 <https://doi.org/10.1016/j.jece.2023.109635>.
- Brillas, E., Serrà, A., Garcia-Segura, S., 2021. Biomimicry designs for photoelectrochemical systems: strategies to improve light delivery efficiency. *Curr. Opin. Electrochem.* 26, 100660 <https://doi.org/10.1016/j.coelec.2020.100660>.
- Bui, D.P., Nguyen, T.D., Le Vo, T.T., Cao, T.M., You, S.J., Pham, V. Van, 2021. SnO<sub>2-x</sub> Nanoparticles decorated on graphitic carbon nitride as S-scheme photocatalysts for activation of peroxymonosulfate. *ACS Appl. Nano Mater.* 4, 9333–9343. <https://doi.org/10.1021/acsanm.1c01801>.
- Dai, J., Wang, Z., Zhu, A., Ji, Y., Kong, Z., Cai, T., Ding, D., 2023. Elimination of sulfadiazine and its metabolite from hydrolyzed urine by biochar activated periodate process: lower environmental risk compared with CoFe<sub>2</sub>O<sub>4</sub>/peroxymonosulfate process. *Chem. Eng. J.* 472, 145080 <https://doi.org/10.1016/j.cej.2023.145080>.
- Diao, Z.H., Lin, Z.Y., Chen, X.Z., Yan, L., Dong, F.X., Qian, W., Kong, L.J., Du, J.J., Chu, W., 2020. Ultrasound-assisted heterogeneous activation of peroxymonosulfate by natural pyrite for 2,4-dichlorophenol degradation in water: synergistic effects, pathway and mechanism. *Chem. Eng. J.* 389, 123771 <https://doi.org/10.1016/j.cej.2019.123771>.
- Du, Y., Ma, W., Liu, P., Zou, B., Ma, J., 2016. Magnetic CoFe<sub>2</sub>O<sub>4</sub> nanoparticles supported on titanate nanotubes (CoFe<sub>2</sub>O<sub>4</sub>/TNs) as a novel heterogeneous catalyst for peroxymonosulfate activation and degradation of organic pollutants. *J. Hazard Mater.* 308, 58–66. <https://doi.org/10.1016/j.jhazmat.2016.01.035>.
- Fedorov, K., Plata-Gryl, M., Khan, J.A., Boczkaj, G., 2020. Ultrasound-assisted heterogeneous activation of persulfate and peroxymonosulfate by asphaltene for the degradation of BTEX in water. *J. Hazard Mater.* 397, 122804 <https://doi.org/10.1016/j.jhazmat.2020.122804>.
- Giannakis, S., Lin, K.Y.A., Ghanbari, F., 2021. A review of the recent advances on the treatment of industrial wastewaters by Sulfate Radical-based Advanced Oxidation Processes (SR-AOPs). *Chem. Eng. J.* 406, 127083 <https://doi.org/10.1016/j.cej.2020.127083>.
- Gómez, E., Cestaro, R., Philippe, L., Serrà, A., 2022. Electrodeposition of nanostructured Bi<sub>2</sub>MoO<sub>6</sub>@Bi<sub>2</sub>MoO<sub>6-x</sub> homojunction films for the enhanced visible-light-driven photocatalytic degradation of antibiotics. *Appl. Catal. B Environ.* 317 <https://doi.org/10.1016/j.apcatb.2022.121703>.
- Guo, R., Wang, Y., Li, J., Cheng, X., Dionysiou, D.D., 2020. Sulfamethoxazole degradation by visible light assisted peroxymonosulfate process based on nano-hybrid manganese dioxide incorporating ferric oxide. *Appl. Catal. B Environ.* 278, 119297 <https://doi.org/10.1016/j.apcatb.2020.119297>.
- Guo, S., Wang, H., Yang, W., Fida, H., You, L., Zhou, K., 2020. Scalable synthesis of Cd-doped α-Fe<sub>2</sub>O<sub>3</sub> with abundant oxygen vacancies for enhanced degradation of organic pollutants through peroxymonosulfate activation. *Appl. Catal. B Environ.* 262, 118250 <https://doi.org/10.1016/j.apcatb.2019.118250>.
- Han, Y., Zhao, C., Zhang, W., Liu, Z., Li, Z., Han, F., Zhang, M., Xu, F., Zhou, W., 2024. Cu-doped CoOOH activates peroxymonosulfate to generate high-valent cobalt-oxo species to degrade organic pollutants in saline environments. *Appl. Catal. B Environ.* 340, 123224 <https://doi.org/10.1016/j.apcatb.2023.123224>.
- Kanarakaju, D., Glass, B.D., Oelgemöller, M., 2018. Advanced oxidation process-mediated removal of pharmaceuticals from water: a review. *J. Environ. Manage.* 219, 189–207. <https://doi.org/10.1016/j.jenvman.2018.04.103>.
- Lee, K.M., Lai, C.W., Ngai, K.S., Juan, J.C., 2016. Recent developments of zinc oxide based photocatalyst in water treatment technology: a review. *Water Res.* 88, 428–448. <https://doi.org/10.1016/j.watres.2015.09.045>.
- Liu, D., Liu, T., Zhang, H., Lv, C., Zeng, W., Zhang, J., 2012. Gas sensing mechanism and properties of Ce-doped SnO<sub>2</sub> sensors for volatile organic compounds. *Mater. Sci. Semicond. Process.* 15, 438–444. <https://doi.org/10.1016/j.mssp.2012.02.015>.
- Ma, Y., Meng, Y., Wang, Z., Xin, Y., Lv, X., Li, Q., Wang, H., Xie, H., Zhang, Z., 2023. In-situ construction of mesoporous CuCo<sub>2</sub>O<sub>4</sub> decorated CNTs networks as a long-lasting peroxymonosulfate activator for rapid removal of aqueous micropollutants. *Chem. Eng. J.* 476, 146694 <https://doi.org/10.1016/j.cej.2023.146694>.
- Ni, T., Yang, Zhibin, Zhang, H., Zhou, L., Guo, W., Liu, D., Chang, K., Ge, C., Yang, Zhijun, 2022a. Visible light assisted peroxymonosulfate activation by NiO/SnO<sub>2</sub> composite for efficient tetracycline degradation. *Appl. Surf. Sci.* 604, 154537 <https://doi.org/10.1016/j.apsusc.2022.154537>.
- Ni, T., Yang, Zhibin, Zhang, H., Zhou, L., Guo, W., Pan, L., Yang, Zhijun, Chang, K., Ge, C., Liu, D., 2022b. Peroxymonosulfate activation by Co<sub>3</sub>O<sub>4</sub>/SnO<sub>2</sub> for efficient degradation of ofloxacin under visible light. *J. Colloid Interface Sci.* 615, 650–662. <https://doi.org/10.1016/j.jcis.2022.02.024>.
- Pang, Y., Zhou, J., Yang, X., Lan, Y., Chen, C., 2021. Rationally designed Co<sub>3</sub>O<sub>4</sub>-SnO<sub>2</sub> activated peroxymonosulfate for the elimination of chloramphenicol. *Chem. Eng. J.* 418 <https://doi.org/10.1016/j.cej.2021.129401>.
- Peng, J., Chang, Y., Xu, L., Zhang, Y., Wang, T., Wang, X., Liu, H., Yan, G., Gao, S., Liu, D., Cao, Z., 2023. Insights into the enhanced removal of sulfamethoxazole via peroxymonosulfate activation catalyzed by bimetallic (Co/Cu) doped graphitic carbon nitride: reaction kinetics, mechanisms, and pathways. *Chem. Eng. J.* 476, 146692 <https://doi.org/10.1016/j.cej.2023.146692>.
- Qi, C., Liu, X., Ma, J., Lin, C., Li, X., Zhang, H., 2016. Activation of peroxymonosulfate by base: implications for the degradation of organic pollutants. *Chemosphere* 151, 280–288. <https://doi.org/10.1016/j.chemosphere.2016.02.089>.
- Rahimzadeh, H., Rahmani, A., Samadi, M.T., Farmany, A., Asgari, G., 2020. Sono-photo-assisted heterogeneous activation of peroxymonosulfate by Fe/CMK-3 catalyst for the degradation of bisphenol A, optimization with response surface methodology. *Water Environ. Res.* 92, 189–201. <https://doi.org/10.1002/wer.1181>.
- Ren, W., Gao, J., Lei, C., Xie, Y., Cai, Y., Ni, Q., Yao, J., 2018. Recyclable metal-organic framework/cellulose aerogels for activating peroxymonosulfate to degrade organic pollutants. *Chem. Eng. J.* 349, 766–774. <https://doi.org/10.1016/j.cej.2018.05.143>.
- Sayadi, M.H., Sobhani, S., Shekari, H., 2019. Photocatalytic degradation of azithromycin using GO@Fe<sub>3</sub>O<sub>4</sub>/ZnO/SnO<sub>2</sub> nanocomposites. *J. Clean. Prod.* 232, 127–136. <https://doi.org/10.1016/j.jclepro.2019.05.338>.
- Serrà, A., Gómez, E., Michler, J., Philippe, L., 2020a. Facile cost-effective fabrication of Cu@Cu<sub>2</sub>O@CuO-microalgae photocatalyst with enhanced visible light degradation of tetracycline. *Chem. Eng. J.* <https://doi.org/10.1016/j.cej.2020.127477>.
- Serrà, A., Pip, P., Gómez, E., Philippe, L., 2020b. Efficient magnetic hybrid ZnO-based photocatalysts for visible-light-driven removal of toxic cyanobacteria blooms and cyanotoxins. *Appl. Catal. B Environ.* 268 <https://doi.org/10.1016/j.apcatb.2020.118745>.
- Shang, J., Zhang, T., Li, X., Luo, Y., Feng, D., Cheng, X., 2023. Mn<sub>3</sub>O<sub>4</sub>-ZnMn<sub>2</sub>O<sub>4</sub>/SnO<sub>2</sub> nanocomposite activated peroxymonosulfate for efficient degradation of ciprofloxacin in water. *Sep. Purif. Technol.* 311, 123342 <https://doi.org/10.1016/j.seppur.2023.123342>.
- Sun, Y., Ma, C., Wu, D., Liu, X., Li, N., Fan, X., Li, Y., Zhang, G., Zhang, F., Peng, W., 2023. Coating CoFe<sub>2</sub>O<sub>4</sub> shell on Fe particles to increase the utilization efficiencies of Fe and peroxymonosulfate for low-cost Fenton-like reactions. *Water Res.* 244, 120542 <https://doi.org/10.1016/j.watres.2023.120542>.
- Takdastan, A., Kakavandi, B., Azizi, M., Golsheh, M., 2018. Efficient activation of peroxymonosulfate by using ferrous oxide supported on carbon/UV/US system: a new approach into catalytic degradation of bisphenol A. *Chem. Eng. J.* 331, 729–743. <https://doi.org/10.1016/j.cej.2017.09.021>.
- Tayyab, M., Kulsoom, U.E., Liu, Y., Mansoor, S., Khan, M., Akmal, Z., Mushtaq, A., Arif, M., Shamriaz, U., Zhou, L., Lei, J., Zhang, J., 2023. Visible light-driven photocatalytic H<sub>2</sub> evolution and dye degradation by electrostatic self-assembly of CdS nanowires on Nb<sub>2</sub>C MXene. *Int. J. Hydrogen Energy* 51, 1400–1413. <https://doi.org/10.1016/j.ijhydene.2023.09.199>.
- Tayyab, M., Liu, Y., Liu, Z., Pan, L., Xu, Z., Yue, W., Zhou, L., Lei, J., Zhang, J., 2022. One-pot in-situ hydrothermal synthesis of ternary In<sub>2</sub>S<sub>3</sub>/Nb<sub>2</sub>O<sub>5</sub>/Nb<sub>2</sub>C Schottky/S-scheme integrated heterojunction for efficient photocatalytic hydrogen production. *J. Colloid Interface Sci.* 628, 500–512. <https://doi.org/10.1016/j.jcis.2022.08.071>.
- Waclawek, S., Lutze, H.V., Grübel, K., Padil, V.V.T., Černík, M., Dionysiou, D.D., 2017. Chemistry of persulfates in water and wastewater treatment: a review. *Chem. Eng. J.* 330, 44–62. <https://doi.org/10.1016/j.cej.2017.07.132>.
- Wang, M., Wang, F., Wang, P., Chu, H., Fu, H., Zhao, C., Wang, C.C., Zhao, Y., 2023. Highly efficient and selective organic pollutants degradation via peroxymonosulfate activation over micron-sized Co-MOF: nearly 100% singlet oxygen mechanism. *Sep. Purif. Technol.* 326, 124806 <https://doi.org/10.1016/j.seppur.2023.124806>.
- Wang, N., Liu, Y., Wu, C., Li, S., Sun, B., Ren, Z., Yi, X.X., Han, X., Du, Y., Wang, J., 2022a. SnO<sub>2</sub> shells-induced rich Co<sup>2+</sup> sites and oxygen vacancies in Fe<sub>x</sub>Co<sub>3-x</sub>O<sub>4</sub> nanocubes: enhanced peroxymonosulfate activation performance for water remediation. *Chem. Eng. J.* 439, 135682 <https://doi.org/10.1016/j.cej.2022.135682>.
- Wang, S., Dong, X., Zheng, N., Wang, Y., Gao, J., 2023. A flexible and easily recyclable polyacrylonitrile/Cd<sub>0.8</sub>Zn<sub>0.2</sub>S/SnO<sub>2</sub> nanofibrous mat for visible-light driven photodegradation of RhB. *Colloids Surfaces A Physicochem. Eng. Asp.* 672, 131755 <https://doi.org/10.1016/j.colsurfa.2023.131755>.
- Wang, T.H., Zhao, Z., Garcia-Segura, S., Ling, L., Doong, R. an, Westerhoff, P., 2024. Flexible fiber photoelectrodes integrating Perovskite-Nafion-ITO layers for efficient photoelectrocatalytic water purification. *Appl. Catal. B Environ.* 342, 123397 <https://doi.org/10.1016/j.apcatb.2023.123397>.
- Wang, W., Song, F., Du, C., Su, Y., 2023. Intercalation of well-dispersed Fe<sub>2</sub>O<sub>3</sub> with SnO<sub>2</sub> toward durable peroxymonosulfate activation to eliminate antibiotics: performance and mechanism. *Chem. Asian J.* 18 <https://doi.org/10.1002/asia.202300085>.
- Wang, W., Song, F., Du, C., Su, Y., 2022b. Durable and eco-friendly peroxymonosulfate activation over cobalt/tin oxides-based heterostructures for antibiotics removal: insight to mechanism, degradation pathway. *J. Colloid Interface Sci.* 625, 479–492. <https://doi.org/10.1016/j.jcis.2022.06.056>.
- Weber, I.T., Valentini, A., Probst, L.F.D., Longo, E., Leite, E.R., 2004. Influence of noble metals on the structural and catalytic properties of Ce-doped SnO<sub>2</sub> systems. *Sensor. Actuatur. B Chem.* 97, 31–38. [https://doi.org/10.1016/S0925-4005\(03\)00577-X](https://doi.org/10.1016/S0925-4005(03)00577-X).
- Xu, L., Wang, X., Sun, Y., Gong, H., Guo, M., Zhang, X., Meng, L., Gan, L., 2020. Mechanistic study on the combination of ultrasound and peroxymonosulfate for the decomposition of endocrine disrupting compounds. *Ultrason. Sonochem.* 60, 104749 <https://doi.org/10.1016/j.ulsonch.2019.104749>.
- Xu, M., Li, J., Yan, Y., Zhao, X., Yan, J., Zhang, Y., Lai, B., Chen, X., Song, L., 2019. Catalytic degradation of sulfamethoxazole through peroxymonosulfate activated with expanded graphite loaded CoFe<sub>2</sub>O<sub>4</sub> particles. *Chem. Eng. J.* 369, 403–413. <https://doi.org/10.1016/j.cej.2019.03.075>.
- Yang, S., Qiu, X., Jin, P., Dzakupas, M., Wang, X.C., Zhang, Q., zhang, L., Yang, L., Ding, D., Wang, W., Wu, K., 2018. MOF-templated synthesis of CoFe<sub>2</sub>O<sub>4</sub> nanocrystals and its coupling with peroxymonosulfate for degradation of bisphenol A. *Chem. Eng. J.* 353, 329–339. <https://doi.org/10.1016/j.cej.2018.07.105>.
- Yang, Z., Zhang, H., Zhou, L., Dong, Z., Wang, Y., Liu, D., Ni, T., 2023. Enhanced activation performance of peroxymonosulfate by NiCo<sub>2</sub>O<sub>4</sub>/SnO<sub>2</sub> composite for

- metronidazole degradation under visible light. *J. Alloys Compd.* 949, 169879 <https://doi.org/10.1016/j.jallcom.2023.169879>.
- Yao, Y., Cai, Y., Wu, G., Wei, F., Li, X., Chen, H., Wang, S., 2015. Sulfate radicals induced from peroxymonosulfate by cobalt manganese oxides ( $\text{Co}_x\text{Mn}_{3-x}\text{O}_4$ ) for Fenton-Like reaction in water. *J. Hazard Mater.* 296, 128–137. <https://doi.org/10.1016/j.jhazmat.2015.04.014>.
- Ye, S., Zeng, G., Tan, X., Wu, H., Liang, J., Song, B., Tang, N., Zhang, P., Yang, Y., Chen, Q., Li, X., 2020. Nitrogen-doped biochar fiber with graphitization from *Boehmeria nivea* for promoted peroxymonosulfate activation and non-radical degradation pathways with enhancing electron transfer. *Appl. Catal. B Environ.* 269, 118850 <https://doi.org/10.1016/j.apcatb.2020.118850>.
- Yue, W., Xu, Z., Tayyab, M., Wang, L., Ye, Z., Zhang, J., 2024. Schottky junction enhanced H<sub>2</sub> evolution for graphitic carbon nitride-NiS composite photocatalysts. *J. Colloid Interface Sci.* 657, 133–141. <https://doi.org/10.1016/j.jcis.2023.11.092>.
- Zhang, W., Zhang, S., Chen, Z., Zhang, Z., 2023. Cobalt-ferrite functionalized graphitic carbon nitride ( $\text{CoFe}_2\text{O}_4$ @g- $\text{C}_3\text{N}_4$ ) nanoconfined catalytic membranes for efficient water purification: performance and mechanism. *J. Mater. Chem. A* 18933–18944. <https://doi.org/10.1039/d3ta03247g>.